

Article

Fully Printed Organic Phototransistor Array with High Photoresponse and Low Power

Yuan Tan ¹, Xinwei Zhang ¹, Rui Pan ¹, Wei Deng ^{1,*}, Jialin Shi ¹, Tianxing Lu ¹, Junye Zhang ¹, Jiansheng Jie ^{1,2} and Xiujuan Zhang ^{1,*}

¹ Jiangsu Key Laboratory for Carbon-Based Functional Materials & Devices, Institute of Functional Nano & Soft Materials (FUNSOM), Soochow University, Suzhou 215123, China

² Macao Institute of Materials Science and Engineering, Macau University of Science and Technology, Macau SAR 999078, China

* Correspondence: dengwei@suda.edu.cn (W.D.); xjzhang@suda.edu.cn (X.Z.)

Abstract: Organic phototransistors (OPTs) as optical chemical sensors have progressed excitingly in recent years, mainly due to the development of new materials, new device structures, and device interfacial engineering. Exploiting the maximum potential of low-cost and high-throughput fabrication of organic electronics and optoelectronics requires devices that can be manufactured in a fully printed way that also have a low operation voltage. In this work, we demonstrate a fully printed fabrication process that enables the realization of a high-yield (~90%) and low-voltage OPT array. By solution printing of a high-quality organic crystalline thin film on the pre-printed electrodes, we create a van der Waals contact between the metal and organic semiconductor, resulting in a small subthreshold swing of 445 mV dec⁻¹ with a signal amplification efficiency over 5.58 S A⁻¹. Our OPTs thus exhibit both a low operation voltage of -1 V and a high photosensitivity over 5.7 × 10⁵, making these devices suitable for a range of applications requiring low power consumption. We further demonstrate the capability of the low-voltage OPT array for imaging and show high imaging contrasts. These results indicate that our fabrication process may provide an entry into integrated and low-power organic optoelectronic circuits fabricated by scalable and cost-effective methods for real-world applications.



Citation: Tan, Y.; Zhang, X.; Pan, R.; Deng, W.; Shi, J.; Lu, T.; Zhang, J.; Jie, J.; Zhang, X. Fully Printed Organic Phototransistor Array with High Photoresponse and Low Power.

Chemosensors **2023**, *11*, 231.

<https://doi.org/10.3390/chemosensors11040231>

Academic Editor: Nicole Jaffrezic-Renault

Received: 28 February 2023

Revised: 3 April 2023

Accepted: 5 April 2023

Published: 7 April 2023



Copyright: © 2023 by the authors. Licensee MDPI, Basel, Switzerland. This article is an open access article distributed under the terms and conditions of the Creative Commons Attribution (CC BY) license (<https://creativecommons.org/licenses/by/4.0/>).

Keywords: full printing; organic phototransistors; low operation voltage; small subthreshold swing; image sensor

1. Introduction

Organic phototransistors (OPTs) adopt a three-terminal transistor device structure that offers an additional gate electric field to magnify the response to incident light, leading to their outstanding performance such as large photosensitivity, high photoresponsivity (R^*), over 100% external quantum efficiency (EQE), and large specific detectivity (D^*) [1–7]. In addition, the fabrication of OPTs is compatible with solution printing technologies, providing additional high-throughput and cost-effective advantages. Combining their superior performance and solution processability, OPTs represent a promising alternative optical detection technology for imaging, optical communications, biomedical monitoring, chemical sensors, and artificial visual-perception systems [1,5,8–11]. Advances in developing novel organic semiconducting materials, designing new device structures, and interfacial engineering have led to unprecedented success in the performance of OPTs, which already can compete with rigid inorganic phototransistors. For instance, by designing a novel hybrid-layered device structure, 2,7-dioctyl[1]benzothieno[3,2-b][1]benzothiophene (C8-BTBT)-based OPT demonstrates an ultra-high photosensitivity of 2.9×10^6 , R of 8.6×10^3 A W⁻¹, D^* of 3.4×10^{14} Jones, and EQE of $2.9 \times 10^6\%$ [12]. Calvi et al. reported a flexible OPT with high stability for photodetection of light intensities as low as few nW cm⁻² [13]. Despite promising advancements, high-performance OPTs usually need to supply a large working

voltage (more than 10 V) [14–21], which leads to a considerable power consumption and inapplicability for battery-powered operation. Furthermore, such high working voltages have difficulty satisfying the demands of flexible/wearable electronic technologies (considering both current flexible battery capacities and safety) [22,23].

Recently, various strategies, such as increasing the capacitance of gate dielectrics and reducing the device trap state density, have been routinely used to lower the operation voltages of OPTs [24–27]. For example, Liu et al. developed a solution-processed high k titanium-silicon oxide/hybrid (hTSO) material to fabricate a high-capacitance dielectric layer and successfully achieved a high R at a low driving voltage of 3 V [28]. In addition, various organic single-crystal materials have been widely adopted as light absorption layers to construct OPTs [29–31]. The use of low-defect organic single crystals not only reduces the trap states within the device channel but can also minimize the interfacial defects between the organic semiconductor and dielectric or contact electrode, enabling low-voltage OPTs. However, fabrication of low-voltage OPTs through the present approaches inevitably involves relatively high vacuum deposition procedures (which greatly loses the advantages of scalable and solution-processable manufacturing of OPTs). Therefore, a fully solution-processed fabrication approach for generating OPTs with low working voltage but high photoresponse performance is needed to move the organic optoelectronic development to real-world device applications.

Here, we report a fully printed fabrication process to achieve a high-yield OPT array with a high photoresponse but low power for an imaging application. In the OPT, van der Waals contacts between metals and semiconductors are created by solution printing of an organic crystalline film on the inkjet-printed electrodes. This preserves the pristine interface between metal and semiconductor, enabling extremely sharp switching characteristics of the device with a small subthreshold swing (SS) of $445 \pm 177 \text{ mV dec}^{-1}$ and a high signal amplification efficiency (A_{eff}) of $5.58 \pm 1.64 \text{ S A}^{-1}$. As a result, the OPTs exhibit excellent optical figures of merit with a high photosensitivity of 5.7×10^5 , a high R of 0.1 A W^{-1} , and a maximum specific detectivity of 1.31×10^9 Jones, respectively, at a very low operation voltage of -1 V . Furthermore, we successfully demonstrate the application of our low-voltage, high-photoresponse OPT array in high-contrast image sensors. Our process offers a general platform for scalable, cost-effective manufacturing of organic optoelectronic devices with both high performance and low power.

2. Materials and Methods

2.1. Materials

The conducting silver (Ag) ink purchased from Shanghai Zhongbin Technology Co., Ltd, Shanghai, China. 2,8-difluoro-5,11-bis-(triethylsilylethynyl)anthradithiophene (Dif-TES-ADT, 99%) was supplied by Luminescence Technology Corp. (Lumtec, Taiwan, China) and used without purification. Pentafluorobenzenethiol (PFBT), poly (4-vinylphenol) (PVP, Mw~11000), poly(melamin-co-formaldehyde) (PMF), and propylene glycol monomethyl ether acetate (PGMEA), and polystyrene (PS, Mw~2000 k) were purchased from Sigma-Aldrich, Burlington, USA. The solvent (m-xylene) was purified and distilled from the drying agents before use.

2.2. Ink Preparation

Fluoropolymer (Cytop) ink was prepared by mixing Cytop (CTL-890 M, Asahi Glass, Tokyo, Japan) and its solvent (CT-Solv. 180, Asahi Glass, Tokyo, Japan) at a volume-to-volume ratio of 8:1. Parylene-C (J&K Scientific, Beijing, China) powders and conductive Ag ink were used directly without treatment. The ink of the dielectric layer was prepared by mixing PVP, PMF, and PGMEA at a weight-to-weight ratio of 0.34:0.16:2.5. PFBT was dissolved in isopropanol at a volume-to-volume ratio of 1:200 to modify the Ag drain/source electrodes. Dif-TES-ADT and PS were dissolved in m-xylene at the same concentration of 10 mg mL^{-1} . Then the two solutions were mixed at a volume-to-volume

ratio of 1:1 to prepare the organic semiconductor ink. All of the inks were prepared at room temperature and stirred for at least 3 h before use.

2.3. Fabrication of the 10×10 OPT Array

Glass substrates were washed with deionized water, acetone, and isopropyl alcohol in an ultrasonic bath for 10 min each. After blow-drying with high-purity nitrogen, all glass substrates were treated in an ultraviolet ozone cleaning system for 30 min. Subsequently, a layer of parylene-C was deposited on the clean substrate by chemical vapor deposition (CVD) to serve as a flattened layer, whose thickness was about 1 μm (Figure S1). Then, the Ag ink was inkjet-printed on the parylene-C films by using an inkjet printer (Scientific3, Shanghai Zhongbin Technology Co., Ltd., Shanghai, China) at a dot-to-dot spacing of 40 μm and heated at 145 $^{\circ}\text{C}$ for 30 min in atmospheric air to obtain the parallel Ag strips. After forming gate electrodes, the PVP ink was blade-coated on the substrate to form a gate dielectric layer. The blade coating conditions for PVP layer were as follows: the substrate temperature was heated at 60 $^{\circ}\text{C}$; the blade coating speed was 12.5 mm s^{-1} ; the gap size between the substrate and blade was set as 100 μm ; and blade tilt angle was 30 $^{\circ}$. After blade coating, the PVP layer was thermally annealed at 160 $^{\circ}\text{C}$ for 2 h in a nitrogen glovebox. The surface topography of the resulting PVP thin film was characterized by atomic force microscopy (AFM, Veeco, Plainview, USA). Then, the Ag ink was patterned with the same process as the gate electrodes to fabricate source/drain electrode pairs. After that, the source/drain electrodes were modified by dipping them into a PFBT/isopropanol solution for 5 min and rinsed with isopropanol. Cytop ink was inkjet-printed between adjacent devices to form superhydrophobic dividing lines, followed by a post-bake at 70 $^{\circ}\text{C}$ for 1 h, allowing the semiconductor material to form patterned films in specified areas. The final step was the fabrication of an organic semiconductor thin film, which was blade-coated with the Dif-TES-ADT/PS blended solution at printing speed of 1.25 mm s^{-1} at 60 $^{\circ}\text{C}$. The characterization of Dif-TES-ADT crystalline films were performed by X-ray diffractometer (XRD, D8 Discover, Bruker, Saarbrücken, Germany) and ultraviolet-visible near-infrared spectrophotometer (Lambda 950).

2.4. OPT Electrical Characterization

The electrical performances of the OPTs were measured by a semiconductor parameter analyzer (Keithley, 4200-SCS, Columbus, USA) equipped with a probe station under ambient conditions. The mobility was extracted from the saturation region by using the equation of $I_{\text{DS}} = (W/2L)C_i\mu(V_G - V_t)^2$. The capacitance per unit area (C_i) of the solution-printed PVP dielectric was measured to be 8.38 nF cm^{-2} (Figure S2). During the light-sensing characteristics, a xenon lamp with tunable light intensities was used as the light source and the intensity was calibrated by a commercial silicon photodetector. To avoid external influences, the light source and device were placed in a shield box. The noise spectral density of the OPT was measured using a semiconductor parameter analyzer (Platform Design Automation, Inc. FS-Pro, Beijing, China) in an electrically and optically shielded box. To demonstrate the imaging function, a number “2” optical image was projected onto the 10×10 OPT array. Then, the current of the 100 OPTs was recorded by manually manipulating the probes and made into maps.

3. Results and Discussion

3.1. Full Printing of the OPT Array

The fully printed fabrication process involves six printing procedures and uses two kinds of solution printing technologies, including inkjet printing and blade coating, as illustrated in Figure 1a. To ensure good substrate flatness, we begin with a parylene-C film-covered glass substrate. First, parallel Ag electrode stripes with an interval of 1760 μm and thickness of 210 nm as the bottom gate electrode array (Figure S3) were deposited on the substrate by inkjet printing (Figure 1(a-i)). Next, a gate PVP dielectric layer was deposited on the Ag electrode array through blade coating technique (Figure 1(a-ii)). The blade-coated

PVP thin film shows a uniform thickness of 318 nm and a smooth surface with a roughness of ~ 0.27 nm rms (Figure S4), providing a good semiconductor-dielectric interface. Then, patterned source (S) and drain (D) electrode pairs were accurately deposited on the top of the gate stripe electrodes by aligning the inkjet-print head (Figure 1(a-iii)), followed by a PFBT solution-modification process. The PFBT could form a chemisorbed monolayer on the Ag surface that would substantially reduce the injection barrier to reduce contact resistance. After that, Cytop ink was inkjet-printed on the sample to form the latticed Cytop lyophobic lines around the patterned S/D electrode pairs (Figure 1(a-iv)). These Cytop lines would resist the successive deposition of organic semiconducting layers and thus can create the patterned structure of organic semiconductors, which can effectively eliminate the “cross-talk” effect between neighboring devices in the array. Finally, organic small-molecule semiconductor, Dif-TES-ADT crystalline film was deposited on the S/D electrode regions through a homemade blade-coating equipment (Figure 1(a-v)) to complete the fabrication of a low-power and high photoresponse OPT array (Figure 1(a-vi)). Figure 1b shows the schematic diagram of our OPT and energy level values, and chemical structure of Dif-TES-ADT. We chosen the blade-coating technique to fabricate the device channel layer since the meniscus could extend from the dielectric surface to the S/D electrode and film growth was not influenced by the differences in surface energy and height between the dielectric and S/D electrodes during blade-coating process [32]. More importantly, directly fabricating an organic semiconductor layer on the S/D electrodes could substantially reduce the disorder and defects at the semiconductor-electrode contact interface, which can help overcome the metal penetration problems of conventional vacuum-deposited organic devices. Since the Dif-TES-ADT crystalline thin film and electrodes were combined with non-bonding van der Waals interactions, the pristine interface has been preserved, which is crucial for achievement of the trap-free organic device.

In this study, Dif-TES-ADT was chosen as the active material for the proof-of-concept since it has excellent adsorption properties in the visible wavelength range and can easily acquire high-crystallinity and oriented thin films through simple solution processing [33,34]. As shown in Figure 1c, the blade-coated Dif-TES-ADT thin film exhibited absorption peaks at wavelengths of about 419, 518, and 546 nm, as was found previously for the Dif-TES-ADT films [33]. Figure 1d shows out-of-plane X-ray diffraction data for the blade-coated Dif-TES-ADT thin film. Diffraction peak at only 5.35° corresponding to (001) plane was observed, confirming the highly oriented Dif-TES-ADT thin film is primarily deposited in the (001) direction. Using the proposed full printing procedures, we demonstrated a 10×10 device array comprising 100 OPTs, indicating that our approach can be readily applied to large-scale device fabrication. As shown in Figure 1e, the OPTs occupy a 2.5×2 cm² area and all of the OPTs have complete components. In a magnified polarized microscopy image of one OPT device among the array, all of the fully patterned and well-aligned electrodes can be clearly seen and the typical channel length and width are 96.75 and 1019.92 μm , respectively. We observed that the Dif-TES-ADT thin film in the channel zone was comprised of large and lamellar-like crystal domains (Figure 1f). The bright color of most of the crystal domains under the polarized optical microscope would disappear when the polarizers’ axis was parallel to the direction of the blade coating (Figure 1g), revealing a well-organized orientation of the grains. Moreover, high-quality Dif-TES-ADT thin film was obtained over the whole area, even if the area includes the patterned S/D electrodes. This is conducive to charge carrier transport and thus can yield an excellent photoresponse performance.

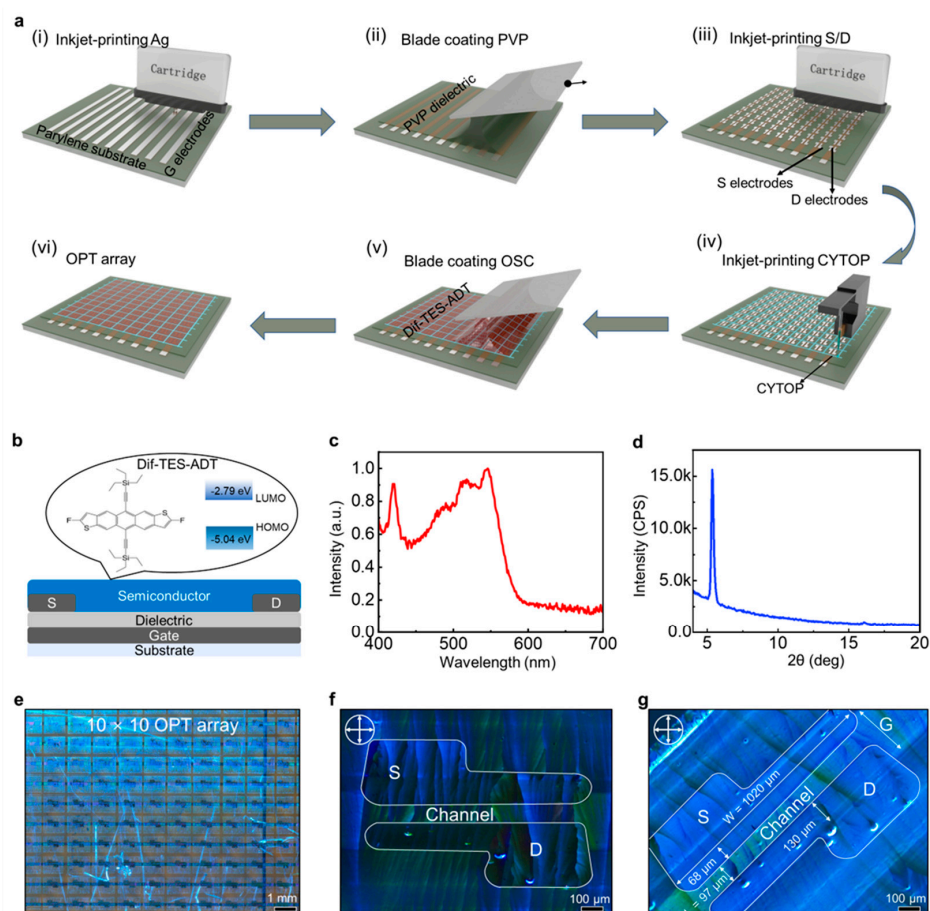


Figure 1. Platform for fabricating the OPT array. (a) Schematic illustrating the flow diagram of the proposed fully printed fabrication process. (a-i) Inkjet-printing gate electrodes. (a-ii) Blade coating PVP dielectric layer. (a-iii) Inkjet-printing source/drain electrodes. (a-iv) Inkjet-printing CYTOP lines. (a-v) Blade coating organic semiconductor film. (a-vi) Obtained OPT array. (b) Schematic cross section of the OPT, energy level values, and chemical structure of Dif-TES-ADT. (c) Absorption spectrum of Dif-TES-ADT crystalline films fabricated by blade coating in the visible wavelength range. (d) XRD spectrum of the blade-coated Dif-TES-ADT. (e) Polarized microscopy image of the device array with 100 OPTs. (f,g) Polarized microscopy images of a representative OPT under different polarization angles 0° and 45° .

3.2. Electrical Performance of the Fully Printed OPT Array

Next, we characterized the electrical properties of the fully printed OPT array by performing systematic tests. Figure 2a shows the transfer curves of 90 (out of 100) OPTs in the dark at a drain voltage of -1 V. 90% of devices presented ideal transistor switching behaviour with an on/off current ratio as high as 10^6 . The output characteristics of a typical OPT device presented in Figure 2b show unambiguous saturation features at a drain voltage > -3 V, indicating the low operation voltage feature of our device. We carried out a statistical analysis of the field-effect mobility and SS of the 90 devices to evaluate the performance uniformity. The average mobilities and SS values are $0.032 \text{ cm}^2 \text{ V}^{-1} \text{ s}^{-1}$ and 445 mV dec^{-1} , respectively; the SS value is much smaller than that of most of the solution-printed organic devices [14–21]. The variations in mobility and SS are 40.6 and 39.6%, respectively, remaining at reasonably low levels (Figure 2c,d). The performance uniformity is partly limited by several practical factors: (1) the variation in the feature size of inkjet-printed Ag electrodes; (2) the alignment offset between the gate electrode and S/D electrodes limited by the unoptimized alignment process with an optical microscope; (3) occasional particle contamination on the sample surface. With further improvement

of inkjet printing technique and apparatus, we expect these practical challenges could be largely addressed to considerably improve the performance consistency. Even so, more than half of the devices still have an SS of less than 400 mV dec^{-1} , the small SS proves the high crystallinity of the Dif-TES-ADT channel layer and the high quality of the semiconductor-dielectric interface, which contributes to the low working voltages. More importantly, such small SS would yield a large signal amplification efficiency (A_{eff} , defined as $\ln(10)/\text{SS}$) of $5.58 \pm 1.64 \text{ S A}^{-1}$ (Figure 2e); a high A_{eff} was essential for the OPTs to achieve a high photoresponse at low power. Excellent bias stress stability for the OPT is crucial to ensure photoresponse reliability. To investigate the bias stress stability, the OPTs were measured under positive gate bias and negative bias stress with a long stress time. The transfer characteristics before and after the bias stresses (2000 s and $\pm 2 \text{ V}$) show good overlap without obvious threshold voltage shift (Figure 2f), indicating the good bias stress stability of our OPT. This result also confirms the low defect density within the device [34].

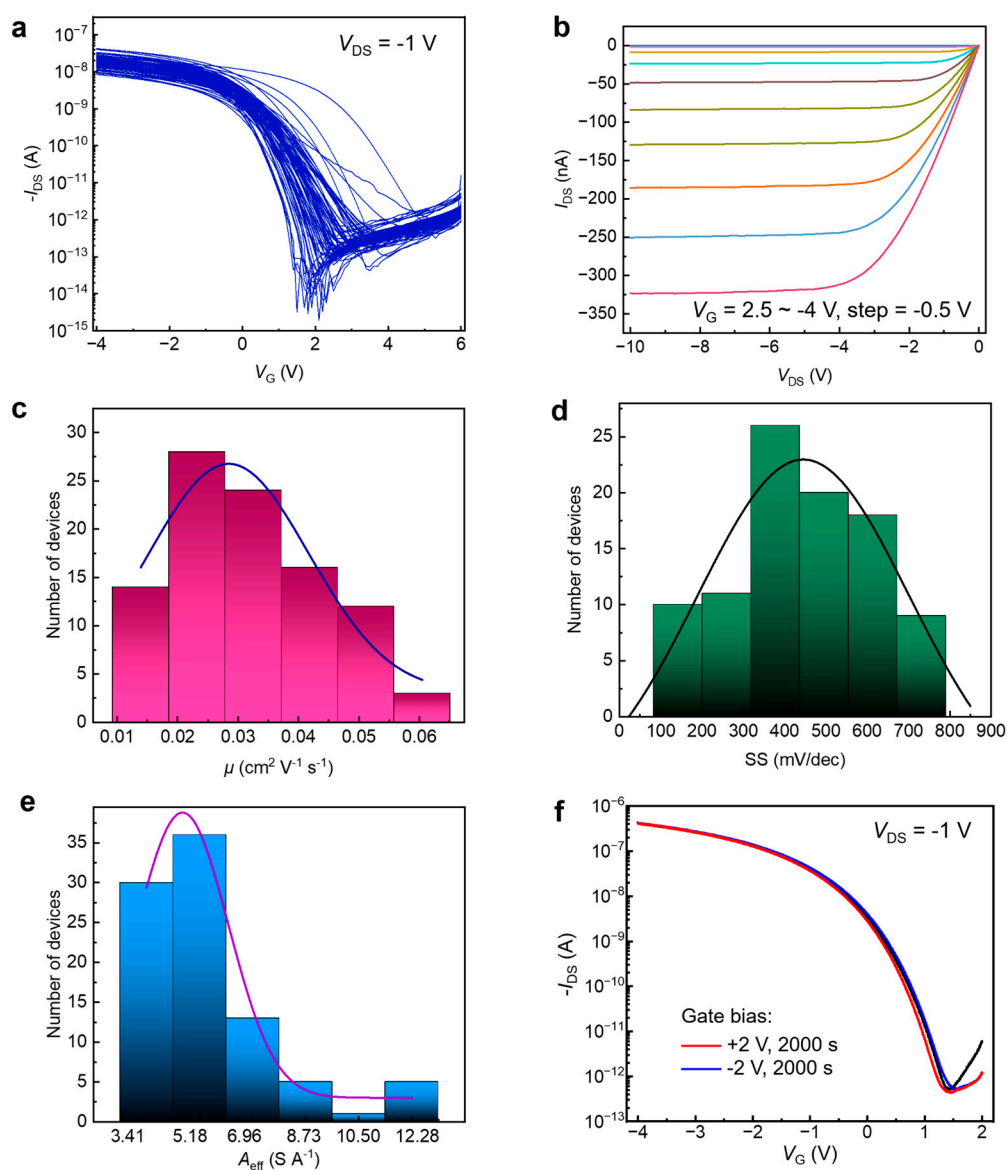


Figure 2. Electrical performance of the fully-printed OPT array in the dark. (a) Transfer characteristics of 90 OPTs in the 10×10 device array. (b) Output curves of a representative OPT in the dark. (c–e) Distribution of mobility, subthreshold swing, and signal amplification efficiency measured over 90 OPTs. (f) Transfer characteristics of a typical OPT measured at gate bias stress.

3.3. Photoresponse of the Fully Printed OPTs

The photoresponse of the fully-printed, low-voltage OPTs was investigated systematically by using a white light source with different incidence light intensities. Upon light irradiation, photogenerated carriers would generate within the Dif-TES-ADT light absorption layer. Owing to the longer lifetime of the electrons in the Dif-TES-ADT, they would be trapped in the Dif-TES-ADT and induce a space-negative charge layer, which could trigger a photogating effect. According to our previous report [3], the density of electron traps buried in the Dif-TES-ADT reaches as high as $8.24 \times 10^{17} \text{ cm}^{-3}$, indicating that abundant photoinduced electrons would be trapped within the Dif-TES-ADT. Under the circumstances, holes would be again injected into the semiconductor channel from the source and move by the S/D electric field. As a result, more holes involved in conductive channel compared to the situation in the dark, producing photocurrent and inducing threshold voltage shifts. Figure 3a exhibits the typical transfer characteristics of the OPT in the dark and under different illumination intensity. From the transfer curves, a positive threshold voltage shift along with a current increase was observed as the light illumination intensity increased, which could be attributed to the trapped photogenerated electrons. In addition, we observed a significant hysteresis in the OPTs under light illumination (Figure S5), which further confirms the existence of a number of electron traps within the bandgap of Dif-TES-ADT [35]. The threshold voltage and photocurrent obtained at gate voltage (V_G) of 2.5 V were plotted as functions of the incident light intensities (Figure 3b). It was found that threshold voltage and photocurrent kept rising with an increase in light illumination. The increased current suggested that a large number of holes produced in the conductive channel, leading to large photoresponse. The maximum photocurrent of 14.34 nA was obtained under a light intensity of $5400 \mu\text{W cm}^{-2}$, suggesting the large photosensitivity of the device. We then calculated the photosensitivity (P), which can be written as $I_{\text{ph}}/I_{\text{dark}}$, where I_{ph} is the photocurrent and I_{dark} is the dark current. Figure 3c depicts the light intensity dependence of the photosensitivity of our OPT device under various V_G . As expected, the photosensitivity at the transistor subthreshold regime is significantly higher than that in other regimes, and the maximum photosensitivity reaches 5.7×10^5 at a light intensity of $5400 \mu\text{W cm}^{-2}$, which is much higher than that of previously reported low-voltage OPTs [24–27]. Especially under weak illumination intensity of $11 \mu\text{W cm}^{-2}$, the P value still exceeded 28.35, proving strong ability of the device to detect dim light.

The R , defined as $I_{\text{ph}}/(P_{\text{light}}S)$, where P_{light} signifies the incident light intensity and S is the effective area of the OPT, is a key parameter to evaluate the photoresponse of the device. The R values of a representative OPT as function of V_G under various light intensities at a fixed V_{DS} of -1 V are presented in Figure 3d. R values follow a continuously increasing trend with the applied V_G . It should be noted that, at the transistor on-state regime, the increasing trend of R values considerably slowed, followed by saturation. When the V_G is -0.6 V and the light intensity is $26 \mu\text{W cm}^{-2}$, R reaches a maximum value of 0.17 A W^{-1} , which is comparable to that of commercial Si photodetectors [36]. The R value for different light intensities is plotted in Figure 3e, showing that the photoresponse of the fully-printed OPT can be effectively modulated by the gate electric field. The R value is raised as the reduced light intensities and the peak of R for our device is 0.17 A W^{-1} . However, for lower light intensity (i.e., $11 \mu\text{W cm}^{-2}$), the R value decreased rather than increased. This is possibly a result of the increased photocarrier recombination probability under the weak light irradiation [37].

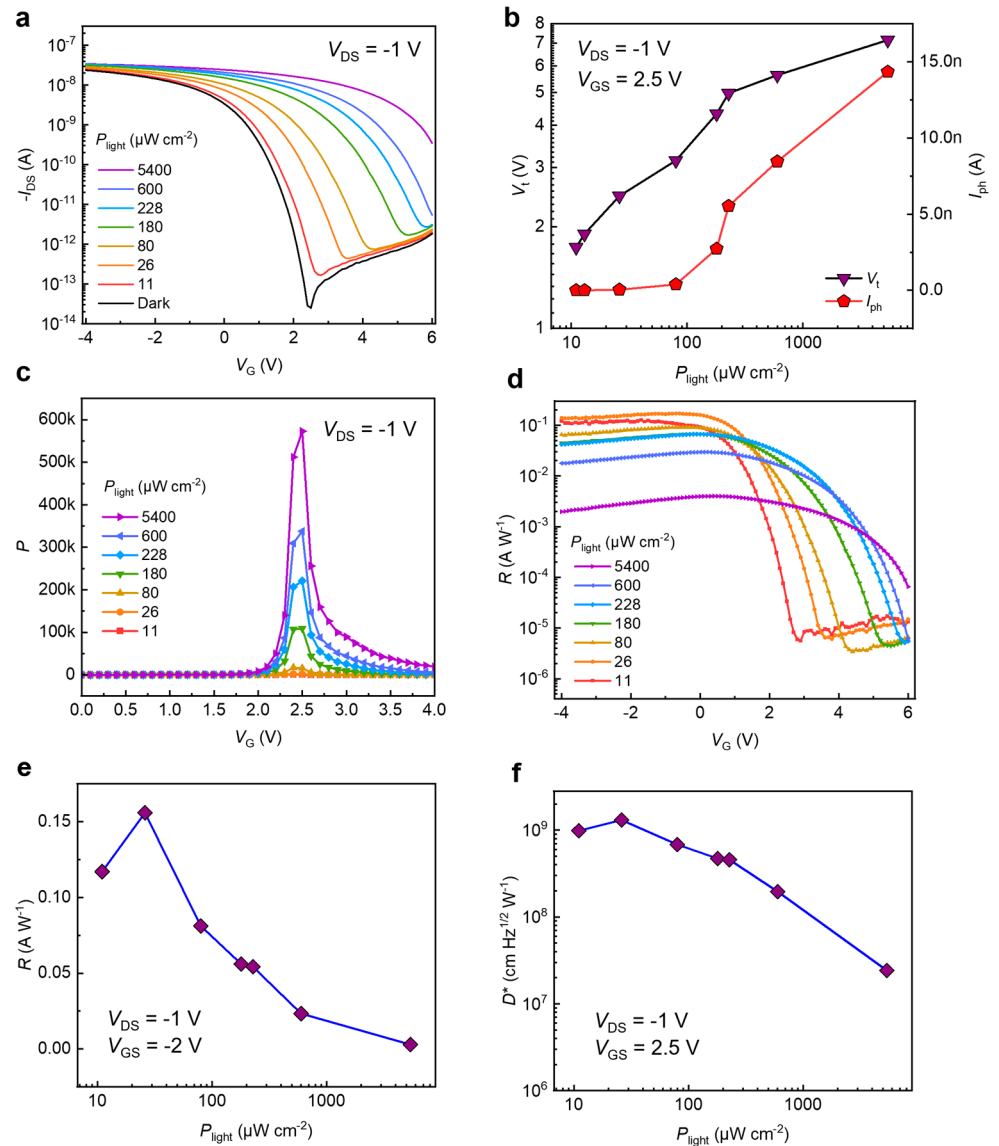


Figure 3. Photoresponse of the fully-printed OPTs. (a) Typical transfer curves of a fully printed OPT in the dark and under light illumination with various intensities. (b) Photocurrent and threshold voltage as a function of the light intensity. Photosensitivity (c) and photoresponsivity (d) as a function of gate voltage under different light intensities. Light intensity-dependent photoresponsivity (e) and specific detectivity (f) of the OPT.

To further assess the device photoresponse performance, we tested the D^* . The D^* represents the capacity of a device to detect weak light signals [11,38,39], which can be expressed as

$$D^* = \frac{\sqrt{SB}}{NEP} \quad (1)$$

where B is the measurement bandwidth and NEP is the noise equivalent power (i_n/R , i_n is the noise current). To accurately calculate the D^* value, we measured the noise spectra of our fully printed OPT (Figure S6). It was found that the device noise was dominated by low-frequency noise, causing by scattering of acoustic phonons and ionized impurities. The i_n was determined to be 3.73 fA Hz^{-1} under $V_G = 2.5 \text{ V}$. The extracted i_n value was rather low, which is consistent with the low dark current of $\sim 0.2 \text{ pA}$ for the fully printed OPT at off state. Then, we calculated the D^* values at different light intensities. The light-intensity-dependent D^* reveals that the fully printed OPT for $B = 1 \text{ Hz}$ exhibits comparatively large

D^* values. Moreover, the D^* shows the same trend with R and reaches a maximum value of 1.3×10^9 Jones at a light intensity of $26 \mu\text{W cm}^{-2}$ (Figure 3f), which is comparable with the reported high-voltage OPTs [40,41].

3.4. Imaging Function Demonstration

As an ultimate proof, we demonstrated the application of the fully printed, low-voltage OPT array in imaging. The OPT array was placed on a shadow mask with hollowed “2” character and a flat light-emitting diode was placed underneath the device array to make pixels zone-selective illumination, as illustrated in Figure 4a. Beforehand, all of the OPTs among the array were measured (Figure S7), and the photoresponse performance and uniformity were evaluated by making statistics on the I_{dark} , I_{ph} , and P . As summarized in Figure 4b, the statistical results show that the I_{dark} and I_{ph} ranged from 16.3 fA to 0.63 pA and 4.04 nA to 17.7 nA, respectively. The average I_{dark} and I_{ph} are 0.162 pA and 10.88 nA, respectively. The calculated P values for the all devices are $>10^4$ and the P values are distributed in a narrow range with a relatively small variable coefficient of 7.9%, indicating good uniformity. This result illustrates that the proposed fully printed fabrication platform has a high yield, stability, and repeatability, allowing us to develop a more complicated circuit. Subsequently, the device imaging capability was examined by projecting the optical number pattern “2” onto the substrate. The current of each pixel in the device array was recorded and the measured current values were converted to a heatmap ranging from black to red. The current signals of pixels shielded by the shadow mask from exposure were in the tens of pA level, while pixels under exposure output signals from 0.168 to 10 nA, which resulted in a distinct signal contrast over two orders of magnitude. Therefore, the imaged number “2” in Figure 4c delivered a high contrast with clear edges. The response speed of a pixel in the OPT array was further measured, revealing a rise time of 2.8 s and a decay time of 0.17 s under a low erasing V_G of 4 V (Figure S8). This speed is reasonable, but the response speed needs to be further improved by shortening the device channel length or introducing a heterojunction for meeting imaging applications [42–44].

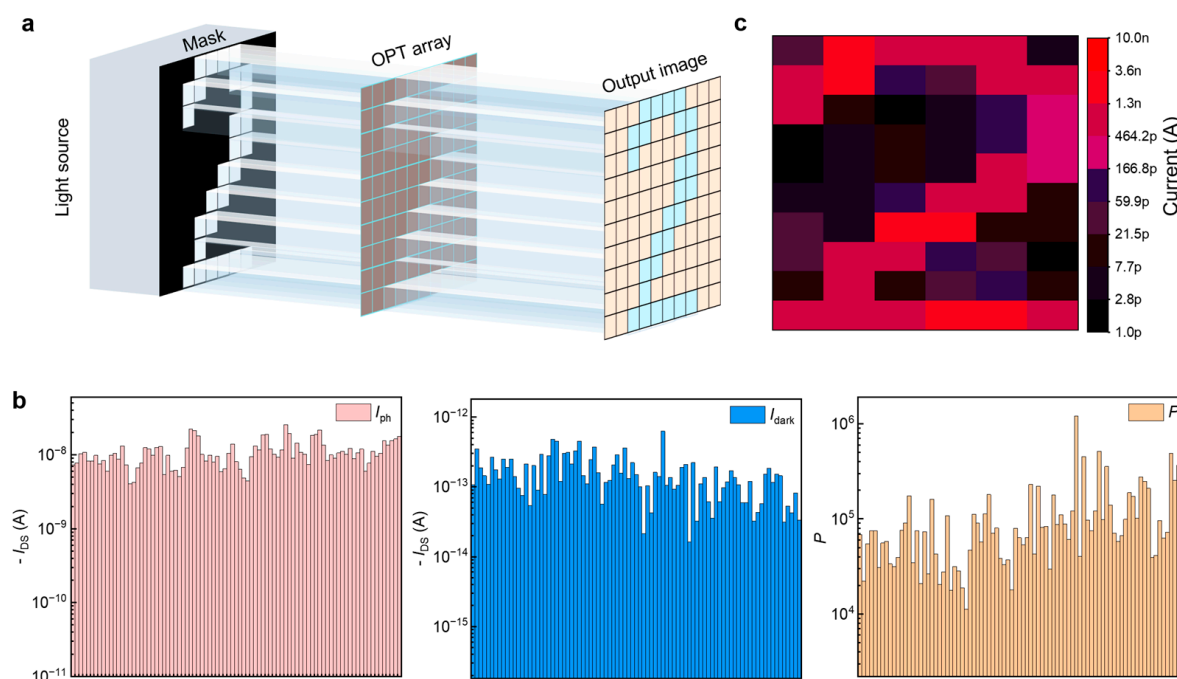


Figure 4. Imaging function demonstration. (a) Schematic diagram illustrating the device arrangement of the OPT array for imaging function. (b) Distribution of the dark, photocurrent, and photosensitivity of the fully printed device array. (c) Reconstructed image of “2” by the OPT array.

4. Conclusions

In summary, we have developed a full printing and facile fabrication process for manufacturing a high-photosensitivity but low-voltage OPT array over a large area. The proposed fully printed procedures involved six solution printing steps and utilized two kinds of solution printing technologies. In particular, by direct solution printing of an organic crystalline thin film on the inkjet-printed electrodes, the interfacial disorder and defects at the semiconductor-electrode contact were reduced. Therefore, the fully printed OPTs realized extremely sharp switching characteristics with a small SS of 445 ± 176 mV dec⁻¹ and a high A_{eff} of 5.45 ± 2.17 S A⁻¹ at a low operation voltage of -1 V. Leveraging the low SS and high A_{eff} , the OPTs exhibited excellent comprehensive performance in terms of a large P of 5.7×10^5 , a reasonable R , and a large D^* . Simultaneously, the OPT array had a >90% device yield and unexpected uniformity with a P variable coefficient of <7.9%, allowing us to demonstrate the high-contrast imaging functions. Our fabrication provides great potential for achieving scalable, cost-effective manufacturing of integrated organic optoelectronic devices with high performance but low power. Additionally, our OPTs provide alternatives for the optoelectronic detection of various chemical signals in ambient.

Supplementary Materials: The following supporting information can be downloaded at: <https://www.mdpi.com/article/10.3390/chemosensors11040231/s1>, Figure S1: 3D morphology of the Parylene-C layer with a thickness of 1.0 μm ; Figure S2: Frequency dependence of capacitance for the blade-coated PVP dielectric. Inset: photograph of the capacitor. Figure S3: (a) Optical image of the inkjet-printed gate electrodes with an interval of 1760 μm . (b) 3D image of the gate electrodes with a thickness of 210 nm. Figure S4: (a) 3D morphology of the blade-coated PVP thin film. (b) Atomic force microscope image of PVP dielectric with a surface roughness of 0.27 nm. Figure S5: Hysteresis of transfer curve of a fully printed OPT under white light illumination. Figure S6: Noise power density of the fully printed OPT at different gate voltage. Figure S7: Transfer characteristics of the OPTs under white light illumination (600 $\mu\text{W}/\text{cm}^2$). Figure S8: Transient photoresponse of the OPT.

Author Contributions: Y.T. and X.Z. (Xinwei Zhang) contributed equally to this work. Conceptualization, W.D., J.J. and X.Z. (Xiujuan Zhang); methodology, Y.T., J.Z. and X.Z. (Xinwei Zhang); validation, X.Z. (Xinwei Zhang), Y.T. and J.Z.; formal analysis, Y.T., X.Z. (Xinwei Zhang) and J.S.; investigation, J.S. and T.L.; data curation, W.D., J.J. and X.Z. (Xiujuan Zhang); writing—original draft preparation, R.P. and J.Z.; writing—review and editing, R.P. and J.S.; visualization, W.D.; supervision, J.J.; project administration, X.Z. (Xiujuan Zhang); funding acquisition. All authors have read and agreed to the published version of the manuscript.

Funding: This research was funded by the National Natural Science Foundation of China (Grant Nos. 52225303, 62274115, 61904117, 51973147, 52173178, and 51821002), Suzhou Key Laboratory of Functional Nano & Soft Materials, Collaborative Innovation Center of Suzhou Nano Science & Technology, the 111 Project.

Institutional Review Board Statement: Not applicable.

Informed Consent Statement: Not applicable.

Data Availability Statement: Not applicable.

Conflicts of Interest: The authors declare no conflict of interest.

References

1. Pierre, A.; Gaikwad, A.; Arias, A.C. Charge-integrating organic heterojunction phototransistors for wide-dynamic-range image sensors. *Nat. Photonics* **2017**, *11*, 193–199. [[CrossRef](#)]
2. Lin, Y.H.; Huang, W.T.; Pattanasattayavong, P.; Lim, J.; Li, R.P.; Sakai, N.; Panidi, J.; Hong, M.J.; Ma, C.; Wei, N.; et al. Deciphering photocarrier dynamics for tuneable high-performance perovskite-organic semiconductor heterojunction phototransistors. *Nat. Commun.* **2019**, *10*, 4475. [[CrossRef](#)] [[PubMed](#)]
3. Ruan, X.B.; Cheng, S.L.; Deng, W.; Tan, Y.; Lu, Z.J.; Shi, J.L.; Zhang, X.J.; Jie, J.S. Insights into the Origins of Minority Carrier Traps in Solution-Processed Organic Semiconductors and Their Effects on Transistor Photostability. *Adv. Electron. Mater.* **2022**, *8*, 2200355. [[CrossRef](#)]

4. Xue, D.; Zhang, Y.Y.; Gong, W.J.; Yin, Y.; Wang, Z.; Huang, L.Z.; Chi, L.F. Interface terminal group regulated organic phototransistors with tunable persistent and switchable photoconductivity. *Sci. China Chem.* **2022**, *65*, 2567–2575. [[CrossRef](#)]
5. He, Z.H.; Shen, H.G.; Ye, D.K.; Xiang, L.Y.; Zhao, W.R.; Ding, J.M.; Zhang, F.J.; Di, C.-a.; Zhu, D.B. An organic transistor with light intensity-dependent active photoadaptation. *Nat. Electron.* **2021**, *4*, 522–529. [[CrossRef](#)]
6. Zhang, L.; Song, L.; Ahn, J.; Han, M.; Linares, M.; Surin, M.; Zhang, H.J.; Oh, J.H.; Lin, J.B. pi-Extended perylene diimide double-heterohelicenes as ambipolar organic semiconductors for broadband circularly polarized light detection. *Nat. Commun.* **2021**, *12*, 142. [[CrossRef](#)]
7. Zhong, J.F.; Wu, X.M.; Lan, S.Q.; Fang, Y.; Chen, H.P.; Guo, T.L. High Performance Flexible Organic Phototransistors with Ultrashort Channel Length. *ACS Photonics* **2018**, *5*, 3712–3722. [[CrossRef](#)]
8. Li, F.; Zheng, L.; Sun, Y.J.; Li, S.Y.; Sun, L.J.; Yang, F.X.; Dong, W.B.; Zhang, X.T.; Hu, W.P. Cocystal engineering: Towards high-performance near-infrared organic phototransistors based on donor-acceptor charge transfer cocrystals. *Sci. China Chem.* **2022**, *66*, 266–272. [[CrossRef](#)]
9. Han, C.; Liu, X.C.; Han, X.W.; He, M.Y.; Han, J.Y.; Zhang, H.; Hou, X.; Zhou, H.X.; Yu, H.; Wu, Z.M.; et al. High-Performance Phototransistor Based on Graphene/Organic Heterostructure for In-Chip Visual Processing and Pulse Monitoring. *Adv. Funct. Mater.* **2022**, *32*, 2209680. [[CrossRef](#)]
10. Deng, W.; Zhang, X.J.; Jia, R.F.; Huang, L.M.; Zhang, X.H.; Jie, J.S. Organic molecular crystal-based photosynaptic devices for an artificial visual-perception system. *NPG Asia Mater.* **2019**, *11*, 77. [[CrossRef](#)]
11. Deng, W.; Lv, Y.; Ruan, X.B.; Zhang, X.J.; Jia, R.F.; Yu, Y.Q.; Liu, Z.K.; Wu, D.; Zhang, X.H.; Jie, J.S. Ultra-Sensitive and Low-Power-Consumption Organic Phototransistor Enables Nighttime Illumination Perception for Bionic Mesopic Vision. *Laser Photonics Rev.* **2022**, *16*, 2200283. [[CrossRef](#)]
12. Gao, Y.H.; Yi, Y.; Wang, X.W.; Meng, H.; Lei, D.Y.; Yu, X.F.; Chu, P.K.; Li, J. A Novel Hybrid-Layered Organic Phototransistor Enables Efficient Intermolecular Charge Transfer and Carrier Transport for Ultrasensitive Photodetection. *Adv. Mater.* **2019**, *31*, e1900763. [[CrossRef](#)]
13. Calvi, S.; Rapisarda, M.; Vellella, A.; Scagliotti, M.; De Rosa, S.; Tortora, L.; Branchini, P.; Mariucci, L. Highly sensitive organic phototransistor for flexible optical detector arrays. *Org. Electron.* **2022**, *102*, 106452. [[CrossRef](#)]
14. Yu, H.Y.; Zhao, X.L.; Tan, M.Y.; Wang, B.; Zhang, M.X.; Wang, X.; Guo, S.L.; Tong, Y.H.; Tang, Q.X.; Liu, Y.C. Ultraflexible and Ultrasensitive Near-Infrared Organic Phototransistors for Hemispherical Biomimetic Eyes. *Adv. Funct. Mater.* **2022**, *32*, 2206765. [[CrossRef](#)]
15. Qin, S.C.; Qin, X.; Du, Q.Q.; Gan, Y.Q.; Zhang, Y.T.; Wang, A.R.; Yan, X.L.; Dong, R.X.; Liu, Y.L.; Li, S.H.; et al. Self-assembled graphene/BUBD-1 hybrids for ultrasensitive organic phototransistors. *J. Mater. Chem. C* **2022**, *10*, 11710–11718. [[CrossRef](#)]
16. Li, H.C.; Jiang, T.; Zheng, Y.S.; Zou, Y.; Qi, S.L.; Tian, G.F.; Ji, D.Y.; Li, L.Q.; Hu, W.P. Fluorinated Dielectrics-Modulated Organic Phototransistors and Flexible Image Sensors. *Adv. Opt. Mater.* **2022**, *10*, 2200614. [[CrossRef](#)]
17. Wang, Z.P.; Liu, J.; Liu, X.S.; Jin, J.Y.; Liu, H.; Peng, K.; Peng, Z.S.; Wei, H.N.; Chu, W.G.; Fan, W.M.; et al. Template-Guided C8-BTBT/MAPbBr₃/C8-BTBT Heterostructures for Broadband Bipolar Phototransistors. *Adv. Mater. Interfaces* **2022**, *9*, 2102344. [[CrossRef](#)]
18. Du, Q.Q.; Qin, S.C.; Wang, Z.F.; Gan, Y.Q.; Zhang, Y.T.; Fan, L.S.; Liu, Y.L.; Li, S.H.; Dong, R.X.; Liu, C.L.; et al. Highly Sensitive and Ultrafast Organic Phototransistor Based on Rubrene Single Crystals. *ACS Appl. Mater. Interfaces* **2021**, *13*, 57735–57742. [[CrossRef](#)]
19. Feng, G.X.; Zhu, M.; Lin, X.H.; Xu, L.; Gao, X.T. Preparation of a CuPc Organic Phototransistor and Research on its Dynamic Photoelectric Properties. *Chem. Mater.* **2021**, *51*, 133–140. [[CrossRef](#)]
20. Huang, H.H.; Jiang, L.; Peng, J.L.; Qi, Y.M.; Bai, S.X.; Lin, Q.Q. High-Performance Organic Phototransistors Based on D18, a High-Mobility and Unipolar Polymer. *Chem. Mater.* **2021**, *33*, 8089–8096. [[CrossRef](#)]
21. Lim, D.H.; Kang, M.; Jang, S.Y.; Hwang, K.; Kim, I.B.; Jung, E.; Jo, Y.R.; Kim, Y.J.; Kim, J.; Choi, H.; et al. Unsymmetrical Small Molecules for Broad-Band Photoresponse and Efficient Charge Transport in Organic Phototransistors. *ACS Appl. Mater. Interfaces* **2020**, *12*, 25066–25074. [[CrossRef](#)]
22. Ren, X.B.; Lu, Z.J.; Zhang, X.J.; Grigorian, S.; Deng, W.; Jie, J.S. Low-Voltage Organic Field-Effect Transistors: Challenges, Progress, and Prospects. *ACS Mater. Lett.* **2022**, *4*, 1531–1546. [[CrossRef](#)]
23. Duan, Y.W.; Zhang, B.W.; Zou, S.Z.; Fang, C.Q.; Wang, Q.J.; Shi, Y.; Li, Y. Low-power-consumption organic field-effect transistors. *J. Phys. Mater.* **2020**, *3*, 014009. [[CrossRef](#)]
24. Yu, F.F.; Wu, S.H.; Wang, X.H.; Zhang, G.B.; Lu, H.B.; Qiu, L.Z. Flexible and low-voltage organic phototransistors. *RSC Adv.* **2017**, *7*, 11572–11577. [[CrossRef](#)]
25. Liu, X.H.; Dong, G.F.; Duan, L.; Wang, L.D.; Qiu, Y. High performance low-voltage organic phototransistors: Interface modification and the tuning of electrical, photosensitive and memory properties. *J. Mater. Chem.* **2012**, *22*, 11836–11842. [[CrossRef](#)]
26. Wu, R.-J.; Hsu, Y.-L.; Chou, W.-Y.; Cheng, H.-L. Enhancing functionalities of organic ultraviolet-visible phototransistors incorporating spiropyran-merocyanine photochromic materials. *J. Mater. Chem. A* **2021**, *9*, 22522–22532. [[CrossRef](#)]
27. Wang, X.H.; Zhu, Y.M.; Wang, G.H.; Qiu, L.Z. Flexible and low-voltage phototransistor based on novel self-assembled phosphonic acids monolayers. *Synthetic Met.* **2020**, *269*, 116563. [[CrossRef](#)]

28. Jiang, B.-Y.; Vegiraju, S.; Chiang, A.S.-T.; Chen, M.-C.; Liu, C.-L. Low-voltage-driven organic phototransistors based on a solution-processed organic semiconductor channel and high k hybrid gate dielectric. *J. Mater. Chem. C* **2017**, *5*, 9838–9842. [[CrossRef](#)]
29. Zhao, C.B.; Ali, M.U.; Ning, J.Y.; Meng, H. Organic single crystal phototransistors: Recent approaches and achievements. *Front. Phys.* **2021**, *16*, 43202. [[CrossRef](#)]
30. Tao, J.W.; Liu, D.; Qin, Z.S.; Shao, B.; Jing, J.B.; Li, H.X.; Dong, H.L.; Xu, B.; Tian, W.J. Organic UV-Sensitive Phototransistors Based on Distriphenylamineethynylpyrene Derivatives with Ultra-High Detectivity Approaching 10¹⁸. *Adv. Mater.* **2020**, *32*, 1907791. [[CrossRef](#)]
31. Zhang, Y.; Qiu, Y.C.; Li, X.Y.; Guo, Y.W.; Cao, S.Q.; Gao, H.F.; Wu, Y.C.; Jiang, L. Organic Single-Crystalline Microwire Arrays toward High-Performance Flexible Near-Infrared Phototransistors. *Small* **2022**, *18*, 2203429. [[CrossRef](#)] [[PubMed](#)]
32. Kitahara, G.; Inoue, S.; Higashino, T.; Ikawa, M.; Hayashi, T.; Matsuoka, S.; Arai, S.; Hasegawa, T. Meniscus-controlled printing of single-crystal interfaces showing extremely sharp switching transistor operation. *Sci. Adv.* **2020**, *6*, eabc8847. [[CrossRef](#)] [[PubMed](#)]
33. Deng, W.; Lei, H.M.; Zhang, X.J.; Sheng, F.M.; Shi, J.L.; Zhang, X.L.; Liu, X.Y.; Grigorian, S.; Zhang, X.H.; Jie, J.S. Scalable Growth of Organic Single-Crystal Films via an Orientation Filter Funnel for High-Performance Transistors with Excellent Uniformity. *Adv. Mater.* **2022**, *34*, 2109818. [[CrossRef](#)] [[PubMed](#)]
34. Park, S.; Kim, S.H.; Choi, H.H.; Kang, B.; Cho, K. Recent Advances in the Bias Stress Stability of Organic Transistors. *Adv. Funct. Mater.* **2020**, *30*, 1904590. [[CrossRef](#)]
35. Iqbal, H.F.; Holland, E.K.; Anthony, J.E.; Jurchescu, O.D. Real-time monitoring of trap dynamics reveals the electronic states that limit charge transport in crystalline organic semiconductors. *Mater. Horizons* **2020**, *7*, 2390–2398. [[CrossRef](#)]
36. Totsuka, D.; Yanagida, T.; Fukuda, K.; Kawaguchi, N.; Fujimoto, Y.; Pejchal, J.; Yokota, Y.; Yoshikawa, A. Performance test of Si PIN photodiode line scanner for thermal neutron detection Nucl. Instrum. Methods Phys. Res. Sect. A **2011**, *659*, 399–402.
37. Ryu, S.; Ha, N.Y.; Ahn, Y.H.; Park, J.Y.; Lee, S. Light intensity dependence of organic solar cell operation and dominance switching between Shockley–Read–Hall and bimolecular recombination losses. *Sci. Rep.* **2021**, *11*, 16781. [[CrossRef](#)]
38. Dou, L.T.; Yang, Y.M.; You, J.B.; Hong, Z.R.; Chang, W.H.; Li, G.; Yang, Y. Solution-processed hybrid perovskite photodetectors with high detectivity. *Nat. Commun.* **2014**, *5*, 5404. [[CrossRef](#)]
39. Guo, N.; Gong, F.; Liu, J.K.; Jia, Y.; Zhao, S.F.; Liao, L.; Su, M.; Fan, Z.Y.; Chen, X.S.; Lu, W.; et al. Hybrid WSe(2)-In(2)O(3) Phototransistor with Ultrahigh Detectivity by Efficient Suppression of Dark Currents. *ACS Appl. Mater. Interfaces* **2017**, *9*, 34489–34496. [[CrossRef](#)]
40. Jung, J.H.; Yoon, M.J.; Lim, J.W.; Lee, Y.H.; Lee, K.E.; Kim, D.H.; Oh, J.H. High-Performance UV-Vis-NIR Phototransistors Based on Single-Crystalline Organic Semiconductor–Gold Hybrid Nanomaterials. *Adv. Funct. Mater.* **2017**, *27*, 1604528. [[CrossRef](#)]
41. Kim, J.; Kim, J.; Jo, S.; Kang, J.; Jo, J.W.; Lee, M.; Moon, J.; Yang, L.; Kim, M.G.; Kim, Y.H.; et al. Ultrahigh Detective Heterogeneous Photosensor Arrays with In-Pixel Signal Boosting Capability for Large-Area and Skin-Compatible Electronics. *Adv. Mater.* **2016**, *28*, 3078–3086. [[CrossRef](#)] [[PubMed](#)]
42. Chen, Y.S.; Yao, Y.F.; Turetta, N.; Samorì, P. Vertical organic transistors with short channels for multifunctional optoelectronic devices. *J. Mater. Chem. C* **2022**, *10*, 2494–2506. [[CrossRef](#)]
43. Yan, Y.J.; Chen, Q.Z.; Wang, X.M.; Liu, Y.Q.; Yu, R.J.; Gao, C.S.; Chen, H.P.; Guo, T.L. Vertical Channel Inorganic/Organic Hybrid Electrochemical Phototransistors with Ultrahigh Responsivity and Fast Response Speed. *ACS Appl. Mater. Interfaces* **2021**, *13*, 7498–7509. [[CrossRef](#)] [[PubMed](#)]
44. Tang, Y.; Fu, H.J.; Li, N.; Hu, Y.H.; Chen, L.X.; Jia, W.Y.; Zhang, Q.M.; Lei, Y.L. Enabling Fast Photoresponse in Near-Infrared Organic Phototransistors by Manipulating Minority Charge Trapping and Recombination. *Adv. Opt. Mater.* **2022**, *11*, 2202008. [[CrossRef](#)]

Disclaimer/Publisher’s Note: The statements, opinions and data contained in all publications are solely those of the individual author(s) and contributor(s) and not of MDPI and/or the editor(s). MDPI and/or the editor(s) disclaim responsibility for any injury to people or property resulting from any ideas, methods, instructions or products referred to in the content.